



Establishing a high-precision real-time ZTD model of China with GPS and ERA5 historical data and its application in PPP

Pengfei Xia¹ · Mengxiang Tong¹ · Shirong Ye¹ · Jingye Qian^{1,2} · Hu Fangxin¹

Received: 1 March 2022 / Accepted: 17 September 2022 / Published online: 7 October 2022
© The Author(s), under exclusive licence to Springer-Verlag GmbH Germany, part of Springer Nature 2022

Abstract

A high-precision real-time troposphere model is constructed by combining ground-based GNSS observation data and the latest European Centre for Medium-Range Weather Forecasts (ECMWF) reanalysis (ERA5). First, the zenith tropospheric delay (ZTD) is extracted in real time with high accuracy by combining the data of more than 500 GNSS stations in the Crustal Movement Observation Network of China (CMONOC) and national reference station network (NRSN); second, a grid model of the elevation normalization model (ENM) in China using ERA5 data is constructed, which takes into account the annual, semiannual and daily cycles. The ZTD estimated by GNSS stations at different heights based on precise point positioning (PPP) is normalized to a uniform height based on ENM; in addition, the optimal smoothing factors of the Gauss distance weighting function in different seasons are determined based on ERA5, which contributes to improved accuracy of ZTD interpolated from GNSS-derived ZTD to ZTD at grid points; finally, a real-time $1^\circ \times 1^\circ$ ZTD grid model of China is created; the broadcast interval is extended to 6 min from few seconds. The new ZTD model has been evaluated using the data of 15 GNSS stations in China in 2020. The test results show that the new ZTD model deviates from the reference value with a mean value better than -0.09 cm and RMSE, better than 1.44 cm compared with the ZTD estimated by post-processing GNSS, while the mean value of the deviation is -0.13 cm, and the RMSE is approximately 3.11 cm compared with radiosonde-derived ZTD. The new ZTD grid model can be used to enhance GNSS/PPP. Two weeks of GNSS observations, one week in winter and another in summer, were randomly collected for PPP processing. The statistical results show the convergence time in the vertical directions is shortened by 37.4% and 38.6% at the 95% and 68% confidence levels after ZTD constraints are applied to the float PPP solution, respectively.

Keywords ZTD model · PPP · ERA5 · Elevation normalization factor model

Introduction

In GNSS high-precision data processing, precise point positioning (PPP) can achieve absolute positioning on a global scale with an accuracy of centimeter level after convergence. However, the method requires a long convergence time to obtain stable positioning results. Therefore, many scholars have tried to shorten the PPP convergence time to promote the application of PPP in GNSS positioning. Currently, additional external atmospheric constraints have been proved to

effectively reduce the PPP convergence time (Li, 2011; Shi, 2014). As a non-dispersive medium, the effects of the troposphere cannot be reduced by a linear combination of different frequency observations as is the case for the ionospheric delay but is generally corrected using empirical models such as the Hopfield, Saastamoinen and the Black models. The three classical models can calculate the real-time zenith dry delay (ZHD) component with an accuracy of millimeters when provided with real-time ground meteorological observation data (Liu et al. 2000; Huang et al. 2020). However, they all have relatively large errors in estimating the zenith wet delay (ZWD) component due to the temporal and spatial variation in water vapor in the atmosphere (Yao et al. 2015; Chen et al. 2015).

Thus, many scholars have focused their research on how to construct an accurate ZWD model. The first approach is to improve the classical models further. For example, Goad

✉ Shirong Ye
srye@whu.edu.cn

¹ GNSS Research Center, Wuhan University, Wuhan 430079, China

² Chinese Antarctic Center of Surveying and Mapping, Wuhan University, Wuhan 430079, China

et al. (1974) modified Hopfield atmospheric refractive index model function by replacing the elevation with the length of the position vector and reconstructing the ZWD model accordingly. The second approach is to envision a new ideal state of the atmosphere under the assumption that the atmospheric temperature decreases linearly with elevation and the wet refractive index at the tropopause is zero, as Berman (1976) developed the "Berman 70" model. Later on, a series of improved models of ZWD were developed, such as "Berman 74," "Berman (TMOD)" and "Berman (D/N)" (Chen et al. 2015); Ifadis (1986) suggested a spatially linear relationship between ZWD and surface meteorological data and developed a new ZWD model accordingly; the third approach is the new ZWD models constructed by Chao (1972), Callahan (1973), Askne and Nordius (1987), Dousa et al. (2014) and Xia et al. (2020), respectively, based on the approximate distribution characteristics of water vapor pressure in the vertical direction. Notwithstanding their different approaches, the ZWD models require the availability of measured meteorological elements, yet many GNSS observation stations are not equipped to take meteorological observations.

Limited by the acquisition of measured meteorological parameters, many scholars have begun to study tropospheric models that do not rely on measured meteorological parameters (Li et al. 2012; Yao et al. 2016; Hadas et al., 2017; Du et al. 2020). Currently, there are two categories of models without meteorological parameter correction: 1. A spatiotemporal model of atmospheric parameters, constructed to compensate for the missing meteorological parameters; 2. The long sequences of ZTD time series fitted as a function of physical factors such as time, geographic location and elevation. Collines and Lengley (1997) constructed UNB3/UNB3m suitable for North America, Penna, et al. (2001) constructed the European EGONS model, Boehm (2007; 2015), Lagler, et al. (2013) constructed the GPT series of global meteorological grid models. To further simplify the calculation of tropospheric delay, some scholars extracted ZTD/ZWD long-term time series based on high-precision numerical meteorological models such as ECWMF, GGOS and NCEP and constructed many ZTD/ZWD empirical grids considering annual, semiannual and diurnal changes. For example, Krueger et al. (2005), Schüler et al. (2014) constructed the TropGrid series, Li et al. (2012) constructed the IGGtrop, Yao et al. (2015, 2016) constructed the GZTD and GZTD2 models, and Huang et al. (2021) constructed the GGZTD model.

Most of the existing ZTD models that do not depend on meteorological parameters are fitted based on ZTD time series extracted from high-precision numerical meteorological models such as NCEP, GGOS and ECWMF, which can only capture the long-term trend of the ZTD model, but cannot perceive the change of ZTD in a short time with a

model accuracy around 4 cm generally (Schüler 2014; Yao, et al. 2015; Huang, et al. 2021). Lou et al. (2018), Zhang et al., (2018) and Zheng et al. (2018) constructed a real-time tropospheric grid model based on the Crustal Movement Observation Network of China (CMONOC) data. However, there is still room for improvement in terms of elevation normalization factor, grid division and broadcast interval. Li et al. (2011) constructed a regional ZTD interpolation model using regional CORS to extract tropospheric delay and used it to enhance PPP positioning, which gradually developed into the PPP-RTK model. Shi et al. (2014) used the OFCs (optimal fitting coefficients) method to fit the ZWD of regional CORS, then broadcasted the model coefficients of the least squares solution to the user and verified the effect of the model in the real-time PPP, which can effectively shorten the convergence time in the elevation direction. Oliveira et al. (2017) adopted the second-order OFCs method and used a more sparse base station network in France to verify the enhancement effect of the ZWD model constructed by this method on real-time PPP. Yao et al. (2017) used the tropospheric ZTD of the GZTD grid as the virtual observation value and used the PPP based on the constraint of the virtual tropospheric ZTD observation value results showing an improvement of about 15% on the convergence time of PPP. Li et al. (2020) divided the tropospheric delay into horizontal and vertical directions and interpolated them, respectively, to verify the correlation between the tropospheric delay and elevation in the vertical direction, using Hong Kong CORS data to verify the improvement in tropospheric-constrained PPP on accuracy and convergence time.

The above studies show that the regional ZTD-enhanced PPP can improve performance in positioning and, more significantly, in height. However, less research has been conducted on the performance of large-scale (1000 km × 1000 km) ZTD grid products in PPP positioning and further evaluation is required. With the increasing demand for high-precision positioning, there is an urgent need for ZTD with higher accuracy, wider regions and stronger real-time performance. Early models developed from the ideal gas equation of state or by fitting long-sequence ZTD can hardly reflect real-time and complex tropospheric atmospheric changes. Therefore, developing high-precision real-time modeling of the troposphere becomes increasingly important.

In this study, more than 500 GNSS stations in CMONOC and the national reference station network (NRSN) are used collectively to improve the distribution density of GNSS stations, while the high-precision and high-resolution ERA5 reanalysis data products are used to construct a grid model of elevation normalization factors in China considering the annual, semiannual and daily cycles, which is to normalize the ZTD estimated by GNSS at different elevations to a same

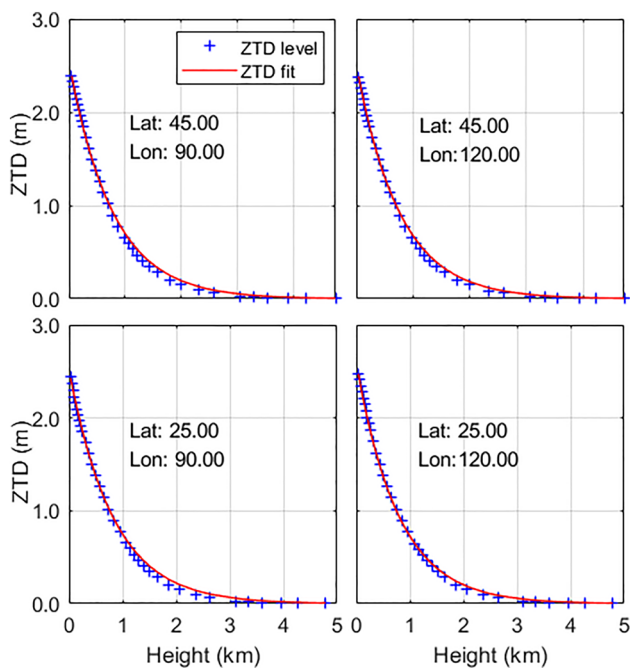


Fig. 1 Trend of ZTD with elevation with different regions in mainland China. ‘ZTD level’ means the ZTD with elevation

height. A Gaussian weighted distance function model is selected to interpolate all the ZTDs estimated by GNSS at a distance of 500 km around a grid point. Then, the smoothing factor in the function is investigated to improve the accuracy of the Gaussian weighted distance function. Finally, a real-time $1^{\circ} \times 1^{\circ}$ ZTD grid model covering China is constructed, and the broadcast interval is extended to 6 min. GNSS data from 15 stations taken in 2020 and the Integrated Global Radiosonde Archive (IGRA) radiosonde dataset are used to test the accuracy of the new model.

We first introduce the data and methods, which describe the process of building ZTD elevation reduction function based on ERA5 product and present the process of establishing the ZTD model with GNSS data. Discussions are presented after that, followed by the conclusions in the last section.

Data and methods

ZTD can be obtained in two methods. One is to take ZTD as the parameter to be estimated, and high-precision ZTD can be obtained by GNSS double-difference or undifferenced methods. The other method is to estimate ZTD by mathematical integration using atmospheric products with high precision and high vertical resolution, such as radiosonde

products, numerical weather forecast products and radio occultation products. The Supplement summarizes the GNSS-PPP and the integral methods using ERA5 numerical meteorological products to obtain ZTD.

Data collection

The fifth-generation reanalysis model (ERA5-<https://apps.ecmwf.int/datasets/data/interim-full-daily>), substituting ERA-Interim after August 31, 2019, is a new climate reanalysis model from ECMWF that takes both models and observations into account to describe the recent climate numerically. Given the spatial resolution of about 25 km, climate variables are estimated hourly. The ERA5 quality-assured monthly update releases with a 3-month delay, while users are provided with preliminary daily updates of the dataset with a 5-day delay. These spatially regular and temporally continuous resolutions and global availability lead to extensive use of the weather model-derived ZTDs not only in meteorology (Lin et al. 2016) but also in geodesy and geophysics, especially to mitigate the atmospheric error in geodetic observations, such as InSAR (Jolivet et al. 2014), GNSS (Zhu et al. 2018) and VLBI (Boehm and Schuh, 2007). The relevant data are free to download at the website (<https://cds.climate.copernicus.eu>). The global mean ZTD difference between ERA5 and GPS is 0.49 cm, while the global standard deviation of the ZTD difference between the weather model of ERA5 and GNSS is 1.69 cm (Yu et al., 2021).

The GNSS data are collected by the China Land State Network and National Geographic Information Bureau, with access to more than 500 stations distributed across the country. The receiver is Trimble NETR9, and the sampling interval of observation files is 30 s, supporting GPS/BDS dual-frequency data. The one-year GNSS observation data for 2020 are collected for the experiment.

Modeling of ZTD elevation normalization factor in mainland China

The elevations of the GNSS stations involved in the modeling vary for some stations having elevation differences of several kilometers. Therefore, it is necessary to normalize the ZTD at all participating stations to the same elevation to eliminate the modeling error caused by the elevation difference. Normally, the elevation naturalization model (ENM) can be constructed by using radiosonde products adjacent to GNSS stations. But due to the limitation of the radiosonde caused by the spatial and temporal resolution, the large-scale

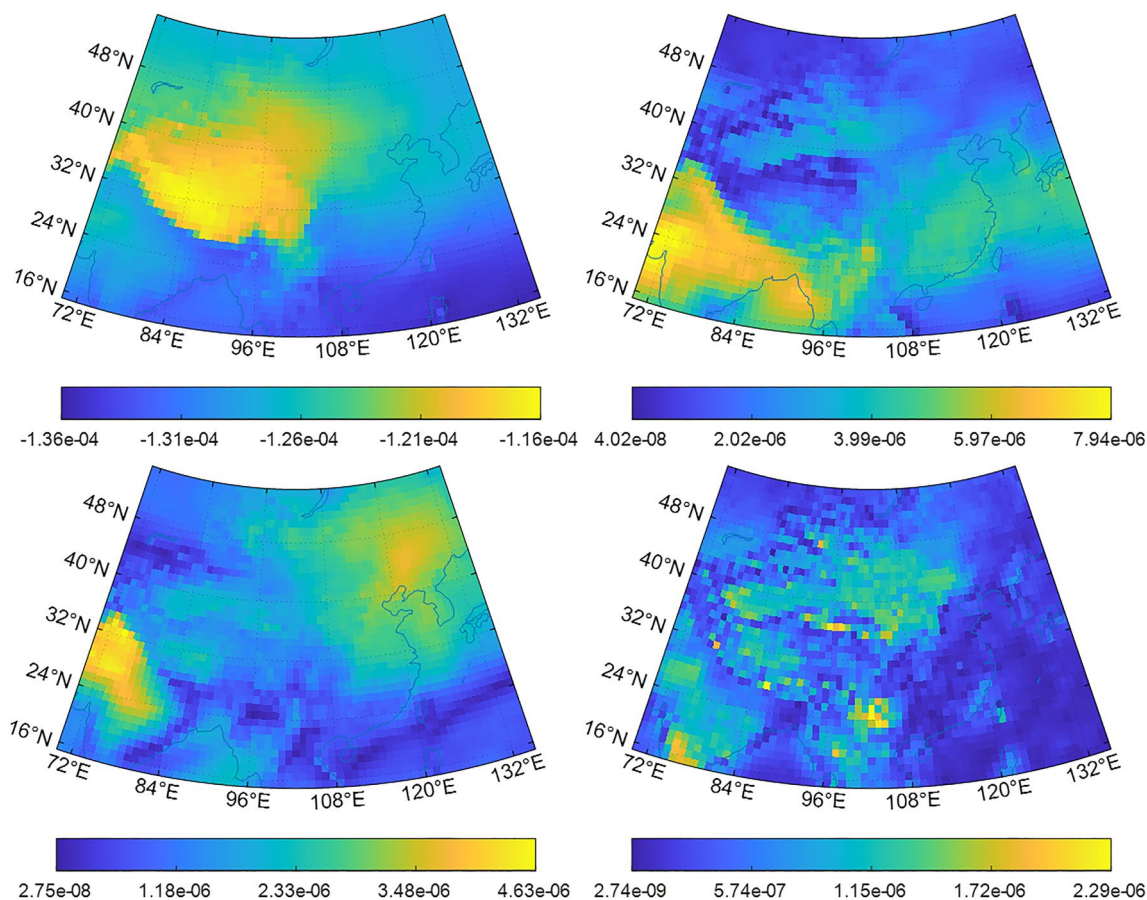


Fig. 2 Mean and period coefficients of the elevation normalization factor. Mean (top left), annual terms (top right), semiannual terms (bottom left) and daily terms (bottom right)

elevation naturalization model will be less accurate. Therefore, the numerical weather model with a high spatial and temporal resolution of ERA5 is used as the modeling data source, and the data for three years 2017, 2018 and 2019, with a temporal resolution of 1 h, a spatial resolution of $1^\circ \times 1^\circ$, a latitude range of 15° - 55° and a longitude range of 70° - 135° are taken for modeling.

Several ZTD profiles at different locations are randomly selected, and curve fitting is performed, as shown in Fig. 1. It can be seen from the figure that the overall ZTD variation with elevation conforms to the negative exponential function model, and therefore, we suggest the negative exponential model is mainly used to fit the elevation variation trend of ZTD. Therefore, the elevation naturalization function of ZTD can be expressed as follows:

$$ZTD = ZTD_s \cdot \exp(b \cdot (h - h_s)) \tag{1}$$

In the above equation, b are the fitting coefficients, also known as the elevation naturalization factor; h_s and ZTD_s are the elevation and ZTD at known stations, respectively. The following equation should be used when the known elevation and ZTD at stations are normalized to the elevation h_0 to be determined:

$$ZTD_0 = ZTD_s \cdot \exp(b \cdot (h_0 - h_s)) \tag{2}$$

It is used to fit the ERA5 data for three consecutive years from 2017 to 2019, and the time series of height reduction factors are calculated for each grid point and fitted using the Fourier series that takes into account the annual, semiannual and daily cycle variations, and the fitting coefficients are solved using least squares and stored at each grid point:

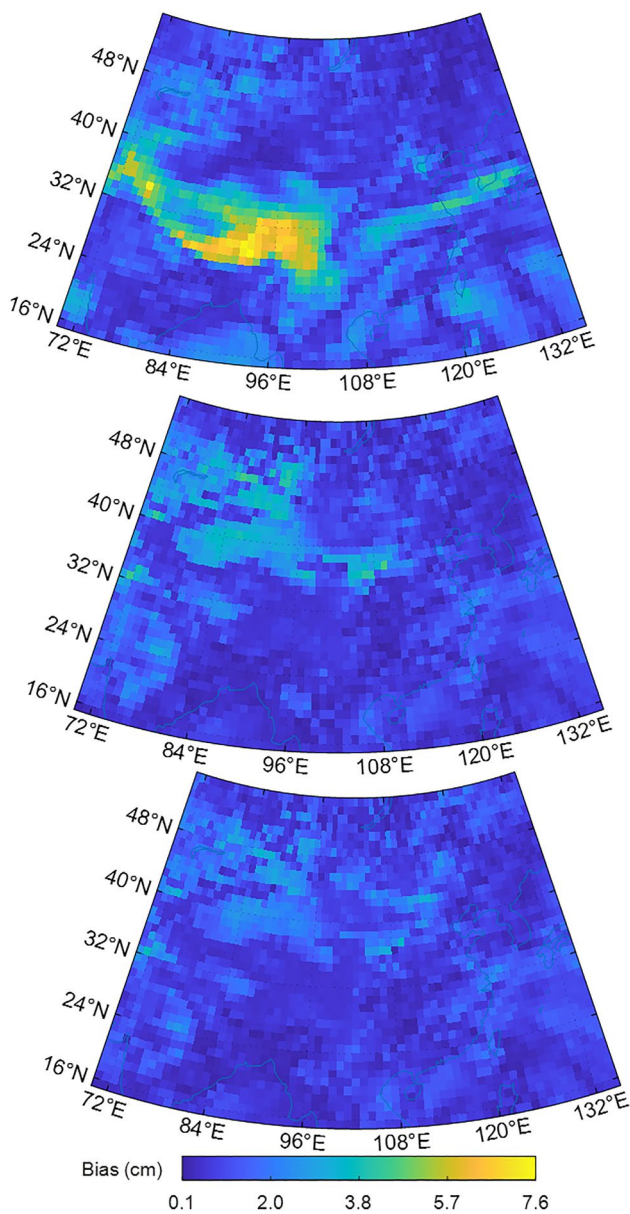


Fig. 3 Mean deviation between EAR5-derived ZTD and ENM-derived ZTD. New empirical ENM (top), new ENM with diurnal variation (middle), new ENM without diurnal variation (bottom)

$$\begin{aligned}
 b = & a_0 + a_1 \cos\left(2\pi \cdot \frac{doy}{365.25}\right) + a_2 \sin\left(2\pi \cdot \frac{doy}{365.25}\right) + a_3 \cos\left(4\pi \cdot \frac{doy}{365.25}\right) + \\
 & a_4 \sin\left(4\pi \cdot \frac{doy}{365.25}\right) + a_5 \cos\left(2\pi \cdot \frac{hod}{24}\right) + a_6 \sin\left(2\pi \cdot \frac{hod}{24}\right) \quad (3)
 \end{aligned}$$

In the above equation, $a_i (i = 0, 1 \dots 6)$ are the model coefficients, doy is the annual cumulative days, and hod is the hours in days.

Figure 2 shows the grid of mean, annual, semiannual and daily terms of the elevation normalization factor. As can be seen, the mean value of the elevation normalization

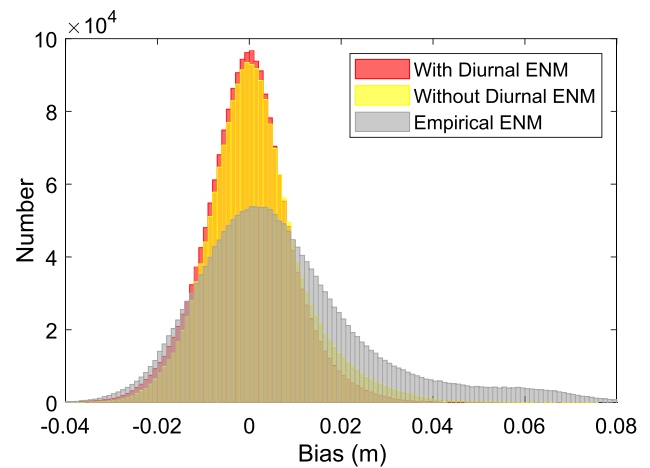


Fig. 4 Distribution of deviation between EAR5-derived ZTD and three ENM-derived ZTD for summer

factor (ENF) is closely related to the elevation of the location, and the absolute value of the ENF is smaller in the Qinghai–Tibet Plateau due to the overall high terrain, scarce water vapor and fewer changes in ZTD in the elevation direction, while the ENF is larger in the low-latitude coastal areas with large water vapor fluctuations. According to the annual cycle and semiannual cycle amplitude, the ENF is mainly related to the seasonal climate of the area. In the southwestern part of the Qinghai–Tibet Plateau, there are multiple monsoonal climates with large fluctuations of rainfall precipitation throughout the year, while in the northeastern part of China, there are high temperatures and rain in summer and cold and dry winters. These diverse climate conditions lead to significant annual and semiannual variations. In contrast, the daily cycle amplitude is more significant in some regions, such as inland rather than coastal areas.

Actually, an empirical ENM has been developed by Dousa et al. (2014) based on UNB3, which requires the surface meteorological parameters. However, the GNSS stations in CMONOC and NRSN are not equipped with meteorological observation instruments. Zheng et al. (2018) proposed to make up for the lack of measured surface meteorological data using the GPT2w model. Then, the new ENM and the empirical ENM are assessed using benchmark values derived from ERA5 in 2020 in China. In addition, in order to analyze the impact of the daily term on the new ENM, the performance of the new ENM with diurnal variation and without diurnal variation is evaluated, respectively. The mean deviation between ERA5-derived ZTD and ENM-derived ZTD is shown in Fig. 3 in summer in China.

As can be seen from Fig. 3, the accuracy of the new ENM with a diurnal variation or without diurnal variation is better than that of the empirical ENM model. The mean deviation

Table 1 Accuracy statistics of the three ENM methods in different seasons (Unit: cm)

	Empirical ENM		Without diurnal ENM		With diurnal ENM	
	Mean	RMS	Mean	RMS	Mean	RMS
Spring	0.91	1.04	1.04	1.28	1.00	1.26
Summer	1.57	1.76	0.94	1.13	0.89	1.09
Autumn	1.20	1.35	0.86	1.06	0.86	1.04
Winter	0.67	0.77	0.89	1.10	0.86	1.08
Mean	1.09	1.23	0.93	1.14	0.90	1.12

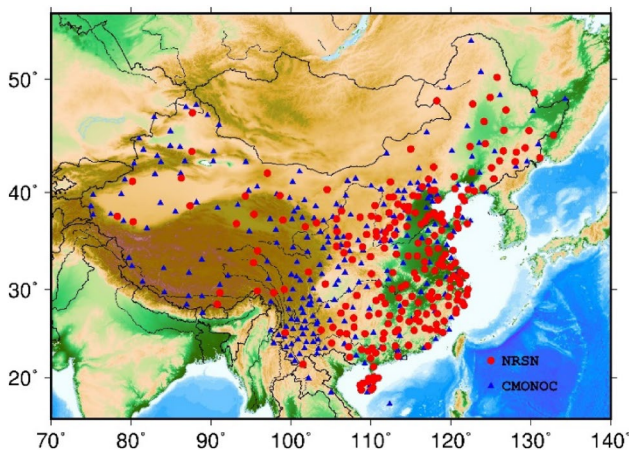


Fig. 5 Distribution of participating modeling GNSS stations

Table 2 Smoothing factor derived by ERA-Interim products at different regions and seasons

Latitude (°)	Season			
	δ (Spring)	δ (Summer)	δ (Autumn)	δ (Winter)
15–25	16.0	13.5	12.5	14.0
25–35	12.5	11.5	13.0	12.5
35–45	11.0	10.5	11.5	11.5
45–55	9.5	10.5	10.5	9.0

between EAR5-derived ZTD and new ENM-derived ZTD is significantly smaller than that of the empirical ENM model in the Qinghai–Tibet Plateau. In addition, the new ENM with diurnal variation is slightly better than that without diurnal variation. Finally, the distribution of deviation between EAR5-derived ZTD and ENM-derived ZTD is shown in Fig. 4 for summer.

Figure 4 illustrates that the deviations between benchmark values and three ENM in summer are normally distributed. In addition, the distribution of deviations between benchmark values and new ENM is mainly concentrated in -0.2 m to 0.4 m, while that of empirical ENM is mainly concentrated in -0.2 m to 0.6 m. Finally, the statistics of

differences between benchmark values and three ENM-derived ZTD in different seasons are listed in Table 1.

Table 1 presents the performance of the ENM for different seasons. It can be noticed that there are no significant differences between the new ENM with diurnal variation and without diurnal variation among the four seasons. From the seasonal statistics of differences, the accuracy of the new ENM with diurnal variation is slightly better than that of the new ENM without diurnal variation. In addition, the accuracy of empirical ENM is better than the new ENM in spring and winter but worse than the new ENM in summer and autumn. According to the statistics for the whole year, the ZTD quality obtained by the new ENM with diurnal variation and without diurnal variation is 8.9% and 7.3% better than that obtained by the empirical ENM, respectively. Considering the performance, it can be concluded that the new ENM with diurnal variation is the optimal ENM for the China region.

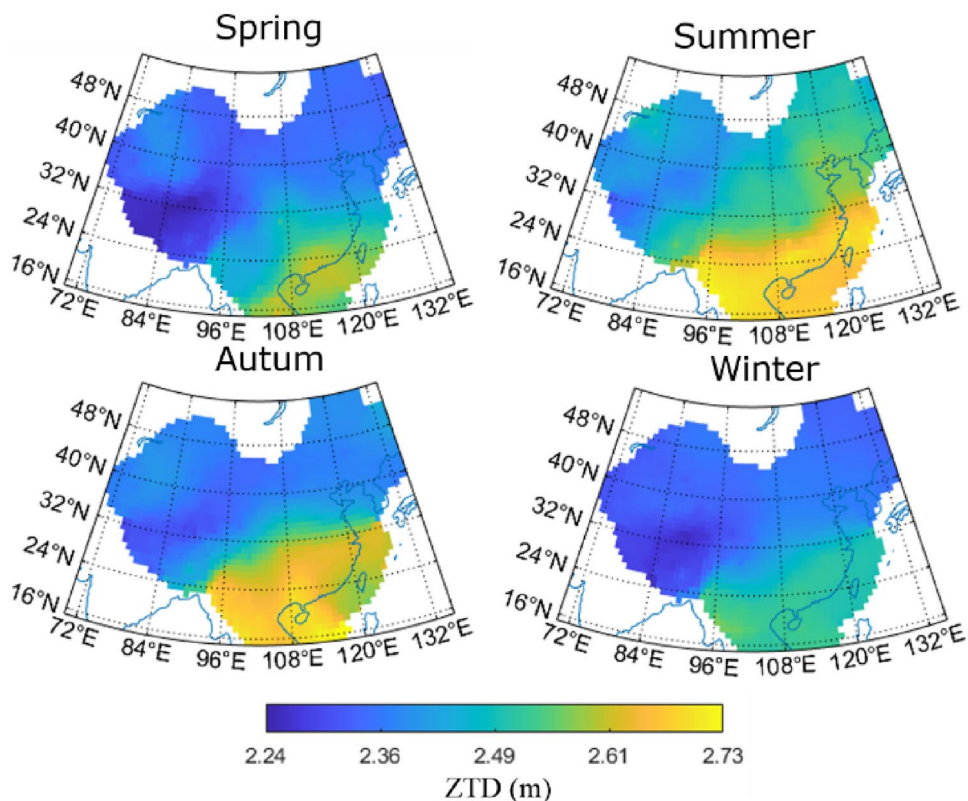
Construction of a regional ZTD grid model in mainland China

The grid with latitude 15° – 55° , longitude 70° – 135° and spatial resolution of $1^\circ \times 1^\circ$ is constructed using the Crustal Movement Observation Network of China and the National Reference Station Network. Figure 5 shows the distribution of the participating modeling stations. More than 500 stations are participating in the modeling, and thus, the overall distribution is relatively uniform in mainland China, where there are more stations in the east than in the west and fewer in the Qinghai–Tibet Plateau.

The ZTD at the modeled stations is normalized to the grid elevation combined with the elevation normalization factor model constructed above. The ZTD at the grid points is interpolated using the Gaussian weighted distance interpolation method to interpolate the ZTD obtained from all GNSS stations within 500 km of the grid points,

$$ZTD_{grid} = \sum_{i=1}^{i=n} \varphi_i ZTD_i \tag{4}$$

Fig. 6 Real-time ZTD grids in China for different seasons



$$\varphi_i = \frac{\exp\left(-\frac{d_i^2}{2\delta^2}\right)}{\sum_{i=1}^{i=n} \exp\left(-\frac{d_i^2}{2\delta^2}\right)} \tag{5}$$

where ZTD_{grid} is the ZTD at the grid point, φ_i is the weight of the i^{th} station, ZTD_i is the ZTD at the grid elevation of the i^{th} station, φ is the Gauss distance weighting function which is based on the principle that the shorter the distance, the stronger the correlation (Xia et al. 2013, 2018), n is the number of the GNSS stations, d_i indicates the distance between GNSS stations and grid and δ denotes the smoothing factor, which will change at different regions. Normally, it is assigned a constant value of experience (Jiang et al. 2014). Because δ varies with regions and seasons, ERA5 data for China from January 2017 to December 2019 are used to precisely estimate δ .

The ZTD of one grid point equals the weighted average of its neighbors (Rius et al. 1997), as follows:

$$0 = \varphi_1 ZTD_1 + \varphi_2 ZTD_2 + \dots + \varphi_{j-1} ZTD_{j-1} - ZTD_j + \varphi_{j+1} ZTD_{j+1} + \dots \tag{6}$$

Equation (6) can be solved by the optimal parameter search method based on the ZTD obtained by ERA5 products with the search step set at 0.5 and the search range to [0, 20], the number of values of δ is exactly the same as that

of grid points, and the mean of δ is defined as the smoothing factor of the level. δ values for different regions and seasons using ERA5 data for China from January 2017 to December 2019 are listed in Table 2. As can be seen from the table, the smoothing factor tends to vary non-linearly across seasons and latitudes. Additionally, the smoothing factors are slightly greater in spring and winter than in summer and autumn and in low latitudes than in high latitudes.

Based on the above, please refer to the Supplement for the specific modeling process and the corresponding flow chart. According to the process above, real-time ZTD grids are constructed for the China region using the real-time orbit and clock difference products recorded by the CNES analysis center, and the ZTD grids are plotted in Fig. 6 by selecting data from different seasons. The average values of ZTD for four seasons, spring, summer, autumn and winter, are shown, respectively. As can be seen from the figure, the ZTD is the largest in summer and the smallest in winter and

falls between these in autumn and spring. Also, the ZTD in the southeastern part of mainland China is larger than that in the northwestern and northeastern regions as a whole and in coastal areas than that in inland areas as a whole. The main reason is that since the ZTD is closely related to the water

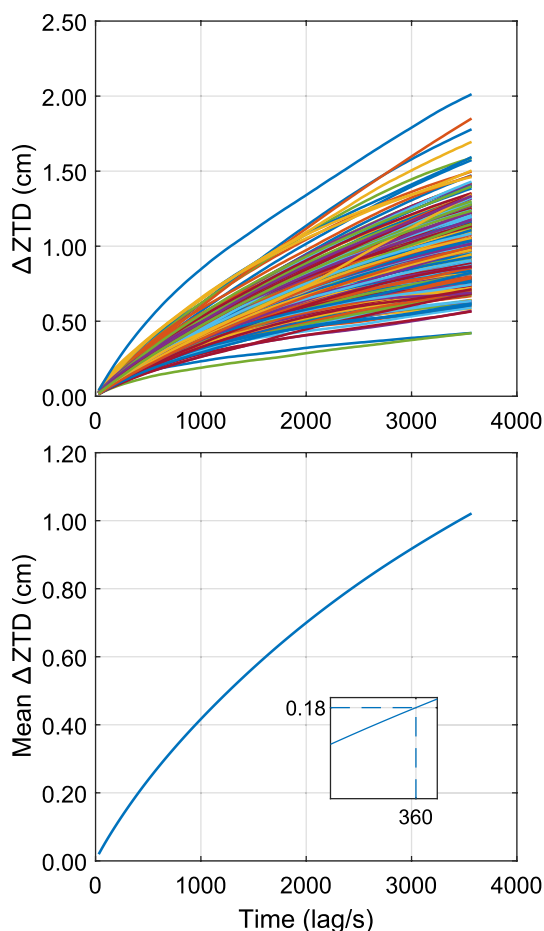


Fig. 7 ZTD deviation for different broadcast intervals. Different broadcast intervals with different stations (top), the mean broadcast interval of different stations (bottom)

vapor content of the place, it varies significantly in different seasons and regions, and the modeling errors caused by it will be different accordingly.

The ZTD models constructed above are all ZTD grids at a certain time, and to ensure real-time application, the grid parameters need to be broadcasted continuously, and a suitable broadcast interval should be set considering the actual demand. The ZTD deviation is 0.18 cm if the slant tropospheric delay (STD) error at 10° altitude angle is less than 1 cm (Oliveira Jr et al., 2017; Chen et al., 2020). Therefore, the ZTD deviation at different intervals of the CMONOC is calculated to determine the appropriate broadcast interval. The first time interval is 30 s, and the second time interval is 60 s. Finally, it stacks up to 3600 s. Then, the mean difference of ZTD between two adjacent epochs is calculated with different time intervals for the whole year of 2020. The following figure shows the distribution of the deviations of

223 CMONOC stations at different intervals and the mean values of the deviations of 223 CMONOC stations at the corresponding intervals.

Figure 7 shows that the overall ZTD error increases with the widening of the broadcast interval. At about 360 s, the average ZTD deviation is 0.18 cm, which meets the requirement of 1 cm for the 10° altitude angle STD error, so 360 s is chosen as the interval of ZTD grid broadcast.

To verify the modeling accuracy, the Bias and RMS at the modeling moment and extrapolation 360 s for all stations are counted, and the accuracy information of spring, summer, autumn and winter is counted according to different seasons, as shown in Fig. 8 and Fig. 9, respectively. It can be seen from the two figures that with the change of seasons, the overall Bias and RMSE of ZTD modeling in summer are larger than those in other seasons, especially in the Yunnan region of China, where both ZTD Bias and RMSE are larger than those in other regions, mainly because of the humid climate and large fluctuations of water vapor in the region, which affect the ZTD modeling accuracy. In addition, the sparse distribution of GNSS stations used for modeling in the region also affects the accuracy of ZTD modeling.

The deviations and RMS of the ZTD model for different months are counted as shown in Tables 3 and 4. The results show that the overall Bias is around -0.1 cm, and the difference between the modeling time and the Bias at the extrapolation of 360 s is not large, while the results of RMS demonstrate that the accuracy of the ZTD grid model is about 1.44 cm, in which the RMS error is the largest in summer and the smallest in winter, with spring and autumn in between. There are more obvious seasonal fluctuations, and the water vapor content in the troposphere varies greatly in summer, making it difficult to model accurately.

Discussion

In order to achieve a statistically meaningful conclusion, the performance of the ZTD model in enhancing real-time PPP can be verified. The precise point positioning method can achieve absolute positioning of a single point without the limitation of the reference station spacing and centimeter-level accuracy after the positioning convergence, with the disadvantage of a long initialization time. The use of external atmospheric products such as tropospheric delay can improve the positioning accuracy and shorten the convergence time to some extent.

Ionospheric-free combined observations are used to eliminate first-order terms, while the previously constructed ZTD

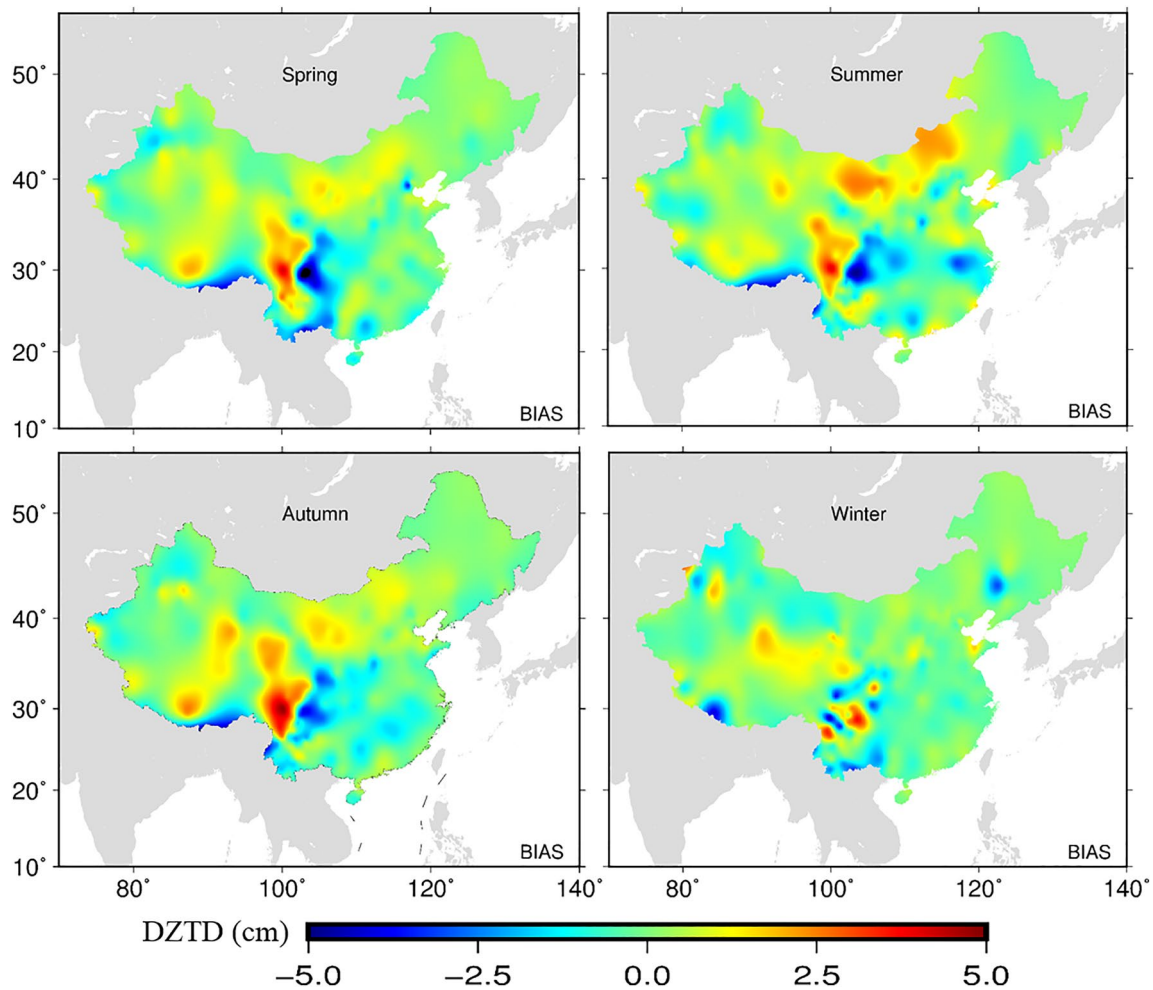


Fig. 8 Deviation between the new model-derived ZTD and the post-process ZTD in mainland China

grid products are used as external virtual observations to verify their effectiveness in precise point positioning, and the corresponding equations are

$$P_{IF} = \rho + cdt_r - cdt^s + T + \varepsilon_{P_{IF}} \tag{7}$$

$$L_{IF} = \rho + cdt_r - cdt^s + T + \lambda_{IF}N_{IF} + \varepsilon_{L_{IF}} \tag{8}$$

$$T_{grid} = T + \varepsilon_T \tag{9}$$

$$R = \begin{bmatrix} \sigma_{P_{IF}} & 0 & 0 \\ 0 & \sigma_{L_{IF}} & 0 \\ 0 & 0 & \sigma_T \end{bmatrix} \tag{10}$$

In the above equation, P_{IF} represents the pseudorange observation of the ionospheric-free combination, L_{IF} is the

ionospheric-free carrier phase observation, ρ is the distance from satellite to receiver, cdt_r is the receiver clock error, cdt^s is the satellite clock error, T is the ZTD, N_{IF} is the ambiguity of ionospheric-free combinations, and λ_{IF} is the wavelength of ionospheric-free combinations. $\varepsilon_{P_{IF}}$, $\varepsilon_{L_{IF}}$ are pseudorange and carrier noise of ionospheric-free combinations, respectively. T_{grid} is the grid ZTD. $\sigma_{P_{IF}}$, $\sigma_{L_{IF}}$, σ_T are the variance of the pseudorange, carrier and grid ZTD, respectively, where the variance of the grid ZTD is given by the statistical results of the ZTD grid accuracy in different seasons in Table 3.

The selected stations are uniformly distributed in the mainland China region and are used as the test stations, as shown in Fig. 10. Details of the strategies and models used in PPP are shown in Table 5.

As convergence is required to extract the ZTD of the GNSS station using real-time PPP, the ZTD extracted after

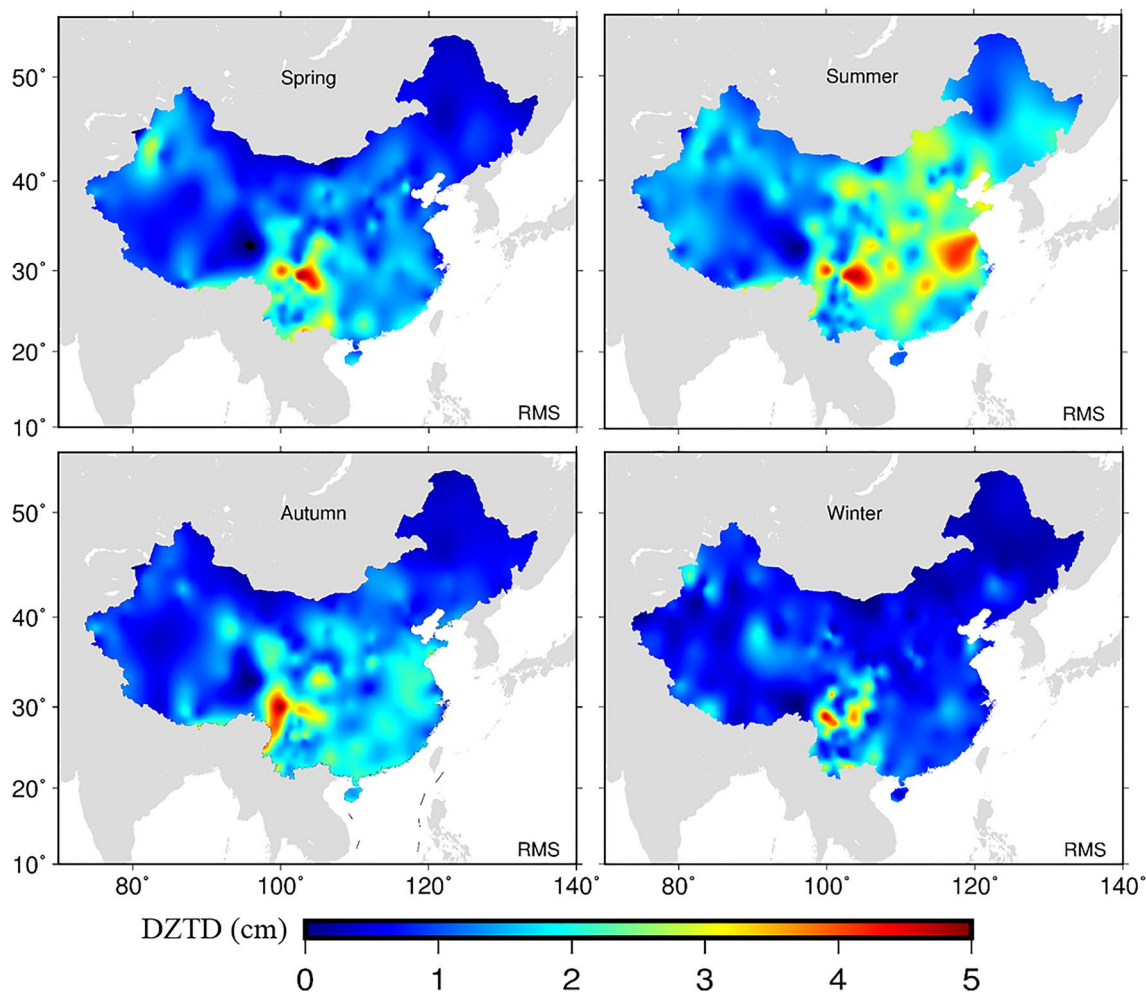


Fig. 9 RMSE of the deviation between the new model-derived ZTD and the post-process ZTD in mainland China

Table 3 Accuracy statistics of ZTD grids in different seasons (Unit: cm)

	Winter		Spring		Summer		Autumn	
	Modeling moments	Outreach 360 s	Modeling moments	Outreach 360 s	Modeling moments	Outreach 360 s	Modeling moments	Outreach 360 s
Bias	-0.12	-0.12	-0.09	-0.11	-0.03	-0.06	-0.08	-0.09
RMSE	0.99	1.0	1.42	1.43	1.90	1.91	1.46	1.47

Table 4 Average accuracy of ZTD grids (Unit: cm)

	Modeling moments	Outreach 360 s
Bias	-0.08	-0.09
RMSE	1.44	1.45

UTC2 time is used to calculate the grid model in this study, and it is used to test the external ZTD constraint of the station. GNSS observations of fourteen random days in 2020 have been processed based on the real-time orbit and clock products, namely one week in winter of DOY 003–009 and another week in summer of DOY 185–191. The accuracy and convergence time of the float PPP solution in E, N and U

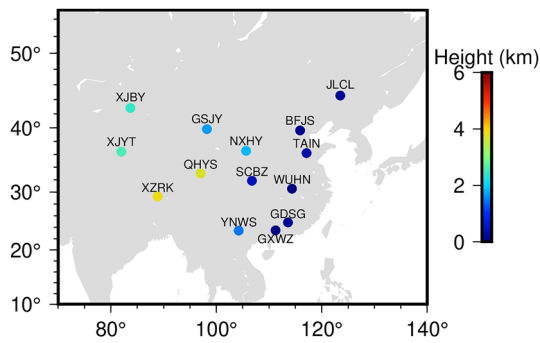


Fig.10 Distribution of stations to test GNSS

directions before (WithoutTrop) and after (WithTrop) applying the ZTD constraint are calculated. Two stations, GSJY and GDSG, are selected from the test stations for analysis, as shown in Figs. 11 and 12.

Figures 11 and 12 illustrate the deviation of the static float PPP solution for two stations. The processing of GNSS observation based on the PPP method with the enhanced ZTD constraints mainly affects the convergence time of the float PPP solution, and there are no significant differences between the float PPP solution with ZTD constraint and without ZTD constraint after the PPP solution converges. Therefore, only part of the positioning results is presented. The figures show that the U-direction convergence time is significantly reduced after applying the enhanced ZTD constraints to the float PPP solution. In addition, the E-direction and N-direction convergence

times are also shortened after applying the enhanced ZTD constraints to the float PPP solution, but that is not obvious. Finally, the convergence times of float PPP solution in horizontal and vertical directions at 95% confidence level and 68% confidence level have been studied, respectively. The convergence time corresponding to the 95% confidence level is defined as the horizontal and vertical deviations less than 0.2 m, and that at 68% confidence level is defined as the horizontal and vertical deviations less than 0.1 m. Then, the statistical results of the convergence times between PPP with ZTD constraint and without ZTD constraint in DOY 003–009 and DOY 185–191 of 2020 are shown in Figs. 13 and 14, respectively.

Figures 13 and 14 show that the convergence time is shortened after the ZTD constraints are applied to the float PPP solution, and the convergence time improved significantly, especially in the vertical direction. In addition, the convergence time also has a certain improvement at the 95% confidence level in winter (DOY 003–009), while that is not significant in summer (DOY 185–191). This can be explained by the fact that the new ZTD grid model has a better modeling performance in winter than in summer. Finally, the statistical results of the convergence time between PPP with ZTD constraint and without ZTD constraint are listed in Table 6.

It can be seen that the convergence times have been shortened by 18.4% and 44% in the horizontal and vertical directions after ZTD constraints are applied on float PPP solution at 95% confidence level in DOY 003–009 of 2020, while these can be shortened by 11.8% and 33.3% at

Table 5 Models and strategies used in PPP

Item	Models
Observations	GPS L1/L2
Satellite orbit and clock	CNES recorded real-time orbit and clock products
Relativistic effects	Corrected
Elevation cutoff angle	10°
Weighting	A priori precision of 0.3 m and 0.003 m for raw code and phase elevation dependent
Ionospheric delay	Ionospheric-free combination
Tropospheric delay	WithoutTrop: ZHD corrected by GPT3, ZWD estimated as random walk noise ($10^{-8} \text{m}^2/\text{s}$) WithTrop: using ZTD grid model
Phase ambiguity	PPP float: not fixed PPPAR: fixed with CNES OSB products
Phase center corrections	igs14.atx
Phase wind up	Corrected
Station displacement	IERS 2003 conventions
Receiver clocks	White noise
DCBs	Corrected with products provided by CODE

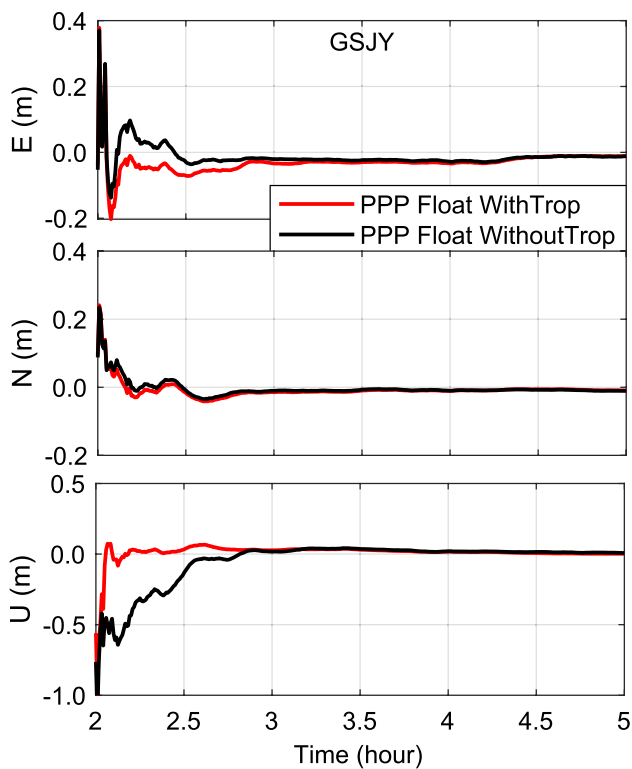


Fig.11 Comparison of E, N and U errors before and after applying the enhanced tropospheric constraints to the float PPP solution at station GSJY in DOY 003 of 2020

68% confidence level, respectively. However, the convergence time in the horizontal direction does not significantly improve after applying ZTD constraints to the float PPP solution in DOY 185–191 of 2020, but in the vertical directions, at the confidence level of 95% and 68%, are shortened by 30.8% and 43.8%, respectively. In all, the convergence time in the vertical directions is shortened by 37.4% and 38.6% at 95% and 68% confidence levels after ZTD constraints are applied to the float PPP solution, respectively.

Conclusion

We present that a ZTD elevation normalization factor grid model for China is constructed using pressure levels data from the ERA5 reanalysis dataset, with a grid range of latitude from 15° to 55° , longitude from 70° to 135° and a resolution of $1^{\circ} \times 1^{\circ}$. The elevation normalization factor time series at each grid point is fitted with Fourier series that consider annual, semiannual and daily cycles, and the model coefficients are solved using least squares and stored at each grid point. The ZTD quality obtained by the new

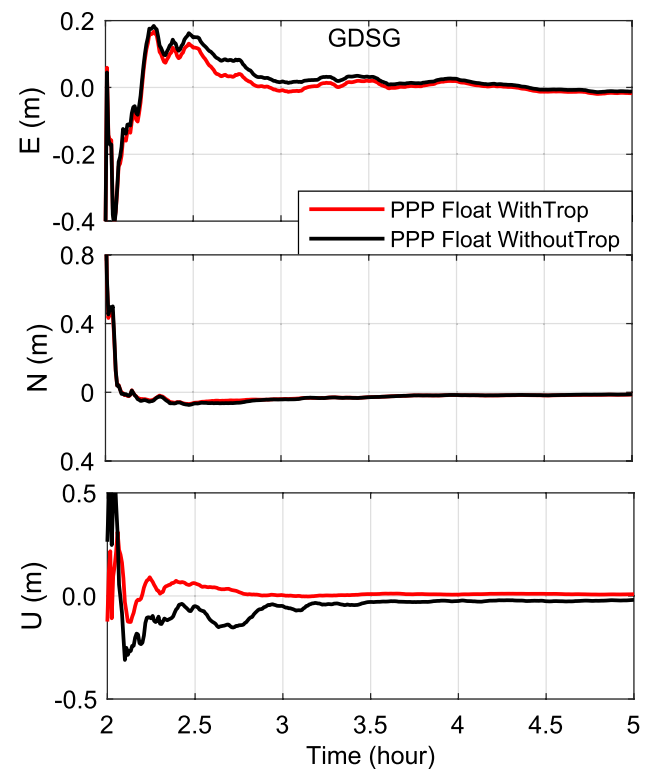


Fig.12 Comparison of E, N and U errors before and after applying the enhanced ZTD constraints to the float PPP solution at station GDSG in DOY 188 of 2020

ENM with diurnal variation and without diurnal variation is 8.9% and 7.3% better than that obtained by the empirical ENM, respectively. By entering the latitude, longitude and time, the user can obtain the local ZTD elevation normalization factor and normalize the ZTDs of different heights to a uniform height. Combining the ZTD estimated by the Crustal Movement Observation Network of China and the national reference station network, a real-time high-precision ZTD grid model for the China region is constructed, with the same grid range as the elevation normalization factor grid. In order to improve the accuracy of interpolation of ZTD obtained from GNSS to ZTD at the grid, the smoothing factor in the Gaussian distance-weighted interpolation model is studied and obtained for different latitudes in different seasons based on ERA5 products. The final constructed ZTD grid model can be broadcasted in 6 min. To verify the outside precision of the new ZTD model, the RMSE values of the deviation of the real-time ZTD grid product from the true value are better than 1.44 cm and 3.11 cm, respectively, by taking the ZTD obtained from the post-processed solution and the ZTD obtained from the radiosonde product as the true value. Data from 15 stations in 2020 were selected to

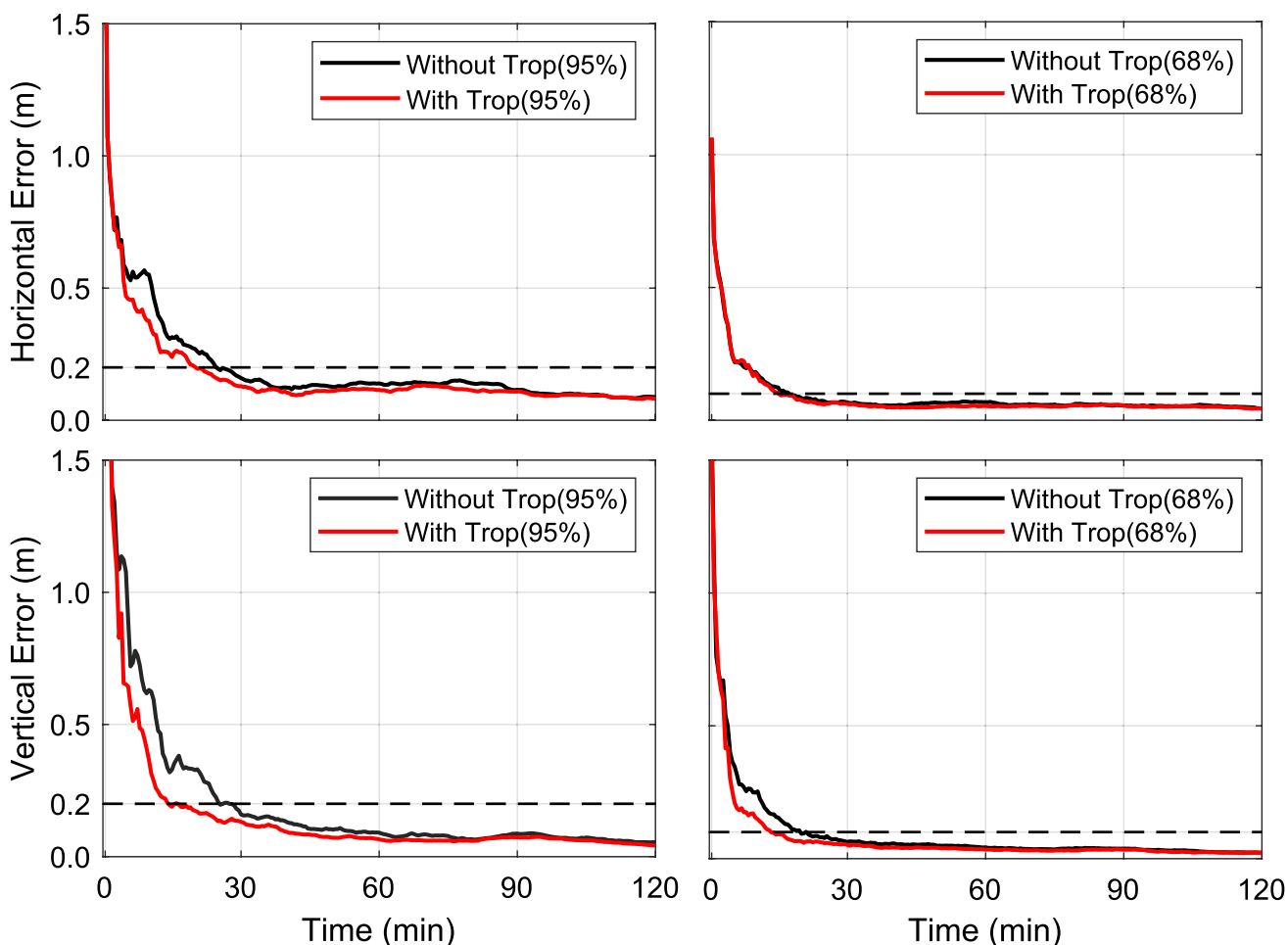


Fig. 13 Convergence times between PPP with ZTD constraint and without ZTD constraint in DOY 003–009 of 2020 at 95% and 68% confidence level

verify the performance of the new ZTD model in enhancing Real-Time PPP. The GNSS observations in DOY 003–009 of 2020 and DOY 185–191 of 2020 were processed using the PPP method with ZTD constraint and without constraint based on real-time orbit and clock products. The statistical results show that the vertical direction convergence time of the float PPP solution with ZTD constraints is reduced by

44% and 33.3% in DOY 003–009 of 2020 at 95% and 68% confidence levels, while these are shortened by 37.4% and 38.6% in DOY 185–191 of 2020, respectively. In the future, with the increase in station density, higher resolution and higher accuracy ZTD grids can be constructed and applied to more fields such as water vapor inversion.

Table 6 Statistics of the convergence time between PPP with ZTD constraint and without ZTD constraint with different confidence levels (Unit: min)

Date	Confidence level	Horizontal		Vertical	
		WithoutTrop	WithTrop	WithoutTrop	WithTrop
DOY (003–009)	95%	24.5	20.0	25.0	14.0
	68%	17.0	15.0	19.5	13.0
DOY (185–191)	95%	15.5	15.5	26.0	18.0
	68%	21.0	19.5	24.0	13.5

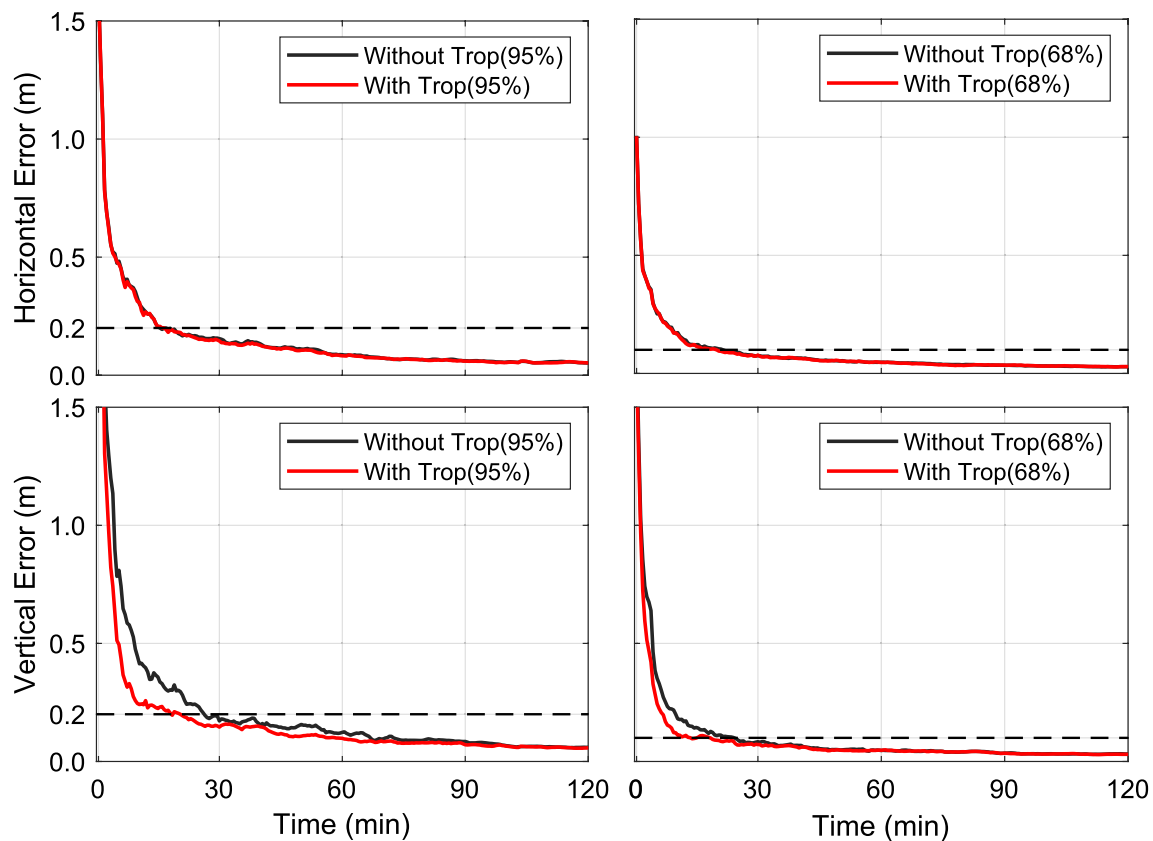


Fig. 14 Convergence times between PPP with ZTD constraint and without ZTD constraint in DOY 185–191 of 2020 at 95% and 68% confidence level

Supplementary Information The online version contains supplementary material available at <https://doi.org/10.1007/s10291-022-01338-9>.

Acknowledgements We thank the National Oceanic and Atmospheric Administration (NOAA) National Centers for Environmental Information (NCEI) for providing the IGRA radiosonde data.

Data availability The fifth generation of the European Centre for Medium-Range Weather Forecasts (ECMWF) reanalysis (ERA5,2022) can also be collected free of charge from <https://apps.ecmwf.int/datasets/data/interim-full-daily>.

References

- Askne J, Nordius H (1987) Estimation of tropospheric delay for microwaves from surface weather data. *Radio Sci* 22(3):379–386. <https://doi.org/10.1029/RS022i003p00379>
- Berman A (1976) The prediction of zenith range refraction from surface measurements of meteorological parameters. Jet Propulsion Laboratory, California Institute of Technology, Pasadena, California, USA, JPL Technical Report 32–1602.
- Boehm J, Schuh H (2007) Troposphere gradients from the ECMWF in VLBI analysis. *J Geodesy* 81:403–408. <https://doi.org/10.1007/s00190-007-0144-2>
- Boehm J, Heinkelmann R, Schuh H (2007) Short Note: A global model of pressure and temperature for geodetic applications. *J Geod* 81:679–683. <https://doi.org/10.1007/s00190-007-0135-3>
- Boehm J, Moeller G, Schindelegger M, Pain G, Weber R (2015) Development of an improved empirical model for slant delays in the troposphere (GPT2w). *GPS Solutions* 19:433–441. <https://doi.org/10.1007/s10291-014-0403-7>
- Callahan P (1973) Prediction of tropospheric wet-component range error from surface measurements. Jet Propulsion Laboratory, California Institute of Technology, Pasadena, California, USA, JPL Technical Report 32–1526.
- Chao CC (1972) A new method to predict wet zenith range correction from surface measurements. Jet Propulsion Laboratory, California Institute of Technology, Pasadena, California, USA, Technical Report 32–1602.
- Chen B, Liu Z (2015) A comprehensive evaluation and analysis of the performance of multiple tropospheric models in China region. *IEEE Trans Geosci* 99:1–16. <https://doi.org/10.1109/TGRS.2015.2456099>
- Chen JP, Wang JG, Wang AH, Ding JS, Zhang YZ (2020) SHAtropE-A regional gridded ZTD model for China and the surrounding areas. *Remote Sensing* 12:165. <https://doi.org/10.3390/rs12010165>
- Collins JP, Langley RB (1997) A tropospheric delay model for the user of the wide area augmentation system, Department of Geodesy and Geomatics Engineering, Final contract report for Nav Canada, Department of Geodesy and Geomatics Engineering Technical Report No. 187, University of New Brunswick, Fredericton, NB, Canada.

- Dousa J, Elias M (2014) An improved model for calculating tropospheric wet delay. *Geophys Res Lett* 41:4389–4397. <https://doi.org/10.1002/2014GL060271>
- Du Z, Zhao QZ, Yao WQ, Yao YB (2020) Improved GPT2w (IGPT2w) model for site specific zenith tropospheric delay estimation in China. *J Atmos Solar Terr Phys* 198:105202. <https://doi.org/10.1016/j.jastp.2020.105202>
- Fifth generation of European Centre for Medium-Range Weather Forecasts (ECMWF) reanalysis (ERA5). The new ECMWF climate reanalysis model, available at: <https://apps.ecmwf.int/datasets/data/interim-full-daily>, last access: February 14, 2022.
- Goad CC, Goodman LL (1974) A modified Hopfield tropospheric refraction correction model, presented at the Fall Annual Meeting American Geophysical Union. California, USA, San Francisco
- Hadas T, Teferle FN, Kazmierski K, Hordyniec P, Bosy J (2017) Optimum stochastic modeling for GNSS tropospheric delay estimation in real-time. *GPS Solut* 21:1069–1081. <https://doi.org/10.1007/s10291-016-0595-0>
- Hopfield HS (1969) Two tropospheric refractivity profile for correcting satellite data. *J Geophys Res* 74:4487–4499. <https://doi.org/10.1029/JC074i018p04487>
- Huang LK, Guo LJ, Liu LL, Chen H, Chen J, Xie SF (2020) Evaluation of the ZWD/ZTD Values Derived from MERRA-2 Global Reanalysis Products Using GNSS Observations and Radiosonde Data. *Sensors* 22(20):6440. <https://doi.org/10.3390/s20226440>
- Huang LK, Chen H, Liu LL, Jiang WP (2021) A new high-precision global model for calculating zenith tropospheric delay. *Chin J Geophys* 64(3):782–795. <https://doi.org/10.6038/cjg202100322>
- Ifadis I (1986) The atmospheric delay of radio waves: Modeling the elevation dependence on a global scale. Tech. Rep. 38L, Sch. of Electrical and comput. Eng., Chalmers Univ. of Technol., Gothenburg, Sweden.
- Jiang P, Ye SR, Liu YY, Zhang JJ, Xia PF (2014) Near real-time water vapor tomography using ground-based GPS and meteorological data: Long-term experiment in Hong Kong. *Ann Geophys* 32:911–923. <https://doi.org/10.5194/angeo-32-911-2014>
- Jolivet R, Agram PS, Lin NY, Simons M, Doin MP, Peltzer G, Li Z (2014) Improving InSAR geodesy using Global Atmospheric Models. *J Geophys Res: Solid Earth* 119:2324–2341. <https://doi.org/10.1002/2013jb010588>
- Krueger E, Schueler T, Hein GW, Martellucci A, Blarmino G (2005) Galileo tropospheric correction approaches developed within GSTB-V1. In Proceedings of ENC-GNSS, 16–19 May, Rotterdam, The Netherlands.
- Lagler K, Schindelegger M, Böhm J, Krásná H, Nilsson T (2013) GPT2: empirical slant delay model for radio space geodetic techniques. *Geophys Res Lett* 40(6):1069–1073. <https://doi.org/10.1002/grl.50288>
- Landskron D, Böhm J (2018) VMF3/GPT3: Refined discrete and empirical troposphere mapping functions. *J Geod* 92:349–360. <https://doi.org/10.1007/s00190-017-1066-2>
- Li XX, Zhang XH, Ge MR (2011) Regional reference network augmented precise point positioning for instantaneous ambiguity resolution. *J Geodesy* 85:151–158. <https://doi.org/10.1007/s00190-010-0424-0>
- Li W, Yuan YB, Ou JK, Li H, Li ZS (2012) A new global zenith tropospheric delay model IGGtrop for GNSS applications. *China Sci Bull* 57:2132–2139. <https://doi.org/10.1360/CSB2012-57-15-1317>
- Li W, Yuan Y, Ou J, Chai Y, Li Z, Liou YA, Wang N (2015) New versions of the BDS/GNSS zenith tropospheric delay model IGGtrop. *J Geodesy* 89:73–80. <https://doi.org/10.1007/s00190-014-0761-5>
- Li YY, Zou X, Tang WM, Deng CL, Wang Y (2020) Regional modeling of tropospheric delay considering vertically and horizontally separation of station for regional augmented PPP. *Adv Space Res* 66:2338–2348. <https://doi.org/10.1016/j.asr.2020.08.003>
- Lin H, You Q, Zhang Y, Jiao Y, Fraedrich K (2016) Impact of large-scale circulation on the water vapor balance of the Tibetan Plateau in summer. *Int J Climatol* 36:4213–4221. <https://doi.org/10.1002/joc.4626>
- Liu YX, Hbiz C, Y. Q. (2000) Precise determination of dry zenith delay for GPS meteorology applications (in Chinese). *Acta Geod Cartography Sin* 29:172–179. <https://doi.org/10.3321/j.issn:1001-1595.2000.02.014>
- Lou YD, Huang JF, Zhang WX, Liang H, Zheng F, Liu JN (2018) A new zenith tropospheric delay grid product for real-time PPP applications over China. *Sensors* 18(1):65. <https://doi.org/10.3390/s18010065>
- Oliveira PS., Morel L, Fund F, Legro R, Monico, JFG, Durand S, Durand F (2017) Modeling tropospheric wet delays with dense and sparse network configurations for PPP-RTK. *GPS Solut.*, 21: 237–250. <https://doi.org/10.1007/s10291-016-0518-0>
- Penna N, Dostson AC, W. (2001) Assessment of EGNOS tropospheric correction model. *The Journal of Navigation* 54(1):37–55. <https://doi.org/10.1017/S0373463300001107>
- Rius A, Ruffini G, Cucurull L (1997) Improving the vertical resolution of ionospheric tomography with GPS occultations. *Geophys Res Lett* 24:2291–2295. <https://doi.org/10.1029/97GL52283>
- Saastamoinen J (1972) Atmospheric correction for the troposphere and stratosphere in radio ranging satellites. *Geophys Monogr Ser* 15:247–251. <https://doi.org/10.1029/GM015p0247>
- Schüler T (2014) The TropGrid2 standard tropospheric correction model. *GPS Solutions* 18(1):123–131. <https://doi.org/10.1007/s10291-013-0316-x>
- Shi JB, Xu CQ, Guo JM (2014) Gao, Y (2014) Local troposphere augmentation for real-time precise point positioning. *Earth, Planets and Space* 66:30. <https://doi.org/10.1186/1880-5981-66-30>
- Xia PF, Cai CS, Liu ZZ (2013) GNSS troposphere tomography based on two-step reconstructions using GPS observations and COSMIC profiles. *Ann Geophys* 31:1–11. <https://doi.org/10.5194/angeo-31-1-1805-2013>
- Xia PF, Ye SR, Jiang P, Pan L, Guo M (2018) Assessing water vapor tomography in Hong Kong with improved vertical and horizontal constraints. *Ann Geophys* 26:969–978. <https://doi.org/10.5194/angeo-36-969-2018>
- Xia P, Xia J, Ye S, Xu C (2020) A new method for estimating tropospheric zenith wet –component delay of GNSS signals from surface meteorology data. *Remote Sensing* 12(21):3497–3517. <https://doi.org/10.3390/rs12213497>
- Yao YB, He CY, Zhang B, Xu CQ (2013) A new global zenith tropospheric delay model GZTD. *Chinese J Geophys* 56:2218–2227. <https://doi.org/10.6038/cjg20130709>
- Yao YB, Yu C, Hu YF (2014) A New Method to Accelerate PPP Convergence Time by using a Global Zenith Troposphere Delay Estimate Model. *The Journal of Navigation* 67:899–910. <https://doi.org/10.1017/S0373463314000265>
- Yao YB, Xu CQ, Shi JB, Yang JJ (2015) ITG: A new global GNSS tropospheric correction model. *Sci Rep* 5:10273. <https://doi.org/10.1038/srep10273>
- Yao Y, Hu Y, Yu C, Zhang B, Guo J (2016) An improved global zenith tropospheric delay model GZTD2 considering diurnal variations. *Nonlinear Process Geophys* 23:127–136. <https://doi.org/10.5194/npg-23-127-2016>
- Yu C, Li ZH, Blewitt G (2021) Global comparisons of ERA5 and the operational HRES tropospheric delay and water vapor products

with GPS and MODIS. *Earth and Space Science* 8:1417. <https://doi.org/10.1029/2020EA001417>

Zhang H, Yuan Y, Li W, Zhang BC, Ou JK (2018) A grid-based tropospheric product for China using a GNSS network. *J Geod* 92:765–777. <https://doi.org/10.1007/s00190-017-1093-z>

Zheng F, Lou YD, Gu SF, Gong XP, Shi C (2018) Modeling tropospheric wet delays with national GNSS reference network in China for BeiDou precise point positioning. *J Geodesy* 92(5):545–560. <https://doi.org/10.1007/s00190-017-1080-4>

Zhu K, Zhao L, Wang W, Zhang S, Liu R, Wang J (2018) Augment BeiDou real-time precise point positioning using ECMWF data. *Earth, Planets and Space* 70:112. <https://doi.org/10.1186/s40623-018-0870-0>

Publisher's Note Springer Nature remains neutral with regard to jurisdictional claims in published maps and institutional affiliations.

Springer Nature or its licensor holds exclusive rights to this article under a publishing agreement with the author(s) or other rightsholder(s); author self-archiving of the accepted manuscript version of this article is solely governed by the terms of such publishing agreement and applicable law.



Pengfei Xia currently is an associate researcher at the GNSS Research Center of Wuhan University, Wuhan, China. He received his Ph.D. from Wuhan University in 2018. His research interests include GNSS data processing and high-precision positioning, and GNSS meteorology.



Mengxiang Tong is a M.Sc. candidate at the GNSS Research Center of Wuhan University, Wuhan, China. His research interests include GNSS data processing and high-precision positioning.



Shirong Ye obtained his Ph.D. from Wuhan University in 2002 and is a professor at the GNSS Research Center of Wuhan University, Wuhan, China. His research interests include precise point positioning (PPP), ground-based GNSS meteorology, and precise GNSS data processing.



Jingye Qian is a M.Sc. candidate at the GNSS Research Center of Wuhan University, Wuhan, China. His main research interests include GNSS data processing of large-scale networks and geodynamics research.



Hu Fangxin is a M.Sc. candidate at the GNSS Research Center of Wuhan University, Wuhan, China. His current research interests are space geodesy and GNSS data processing.